PHYSICAL REVIEW C VOLUME 51, NUMBER 2 FEBRUARY 1995

Isospin character of transitions to the 2_1^+ and 3_1^- states of ^{90,92,94,96}Zr

B. J. Lund, N. P. T. Bateman, and S. Utku
A.W. Wright Nuclear Structure Laboratory, Yale University, New Haven, Connecticut 06511

D. J. Horen and G. R. Satchler
Oak Ridge National Laboratory, Oak Ridge, Tennessee 37831

(Received 15 July 1994)

The elastic and inelastic scattering of 35.4 MeV alpha particles by ^{90,92,94,96}Zr have been measured to investigate the isospin mixing of transitions to the 2_1^+ and 3_1^- states. The data have been analyzed using a deformed optical model potential and a folding model assuming transition densities of either the standard collective model type or resulting from random-phase approximation calculations. For the 2_1^+ states of ^{90,92,94}Zr, both models give $B(E2)\uparrow$ values which are in excellent agreement with those determined from Coulomb excitation or lifetime measurements. Both models of analysis suggest a sharp drop in the $B(E2)\uparrow$ at ^{96}Zr relative to the value at ^{90,92,94}Zr, in agreement with an earlier measurement of alpha-particle scattering. Deduced M_n/M_p ratios for ^{92,94,96}Zr are considerably larger than their respective ratios of N/Z. General agreement is found between folding model calculations for alpha-particle scattering and ^{6}Li scattering when using the same random-phase approximation (RPA) transition densities. A small shift in phase is observed between the oscillations in the calculated inelastic angular distributions and the measured ones. A possible means to reproduce this shift is presented, but the changes required appear to be too large to be physically meaningful.

PACS number(s): 21.10.Hw, 25.55.Ci, 27.60.+j

I. INTRODUCTION

The experimental determination of the isospin character of nuclear transitions can be used to provide a test of nuclear structure calculations. Several such measurements have been made on ^{90,92,94,96}Zr. Rychel *et al.* [1] measured the scattering of 35.4 MeV alpha particles, an energy at which interference effects between the Coulomb and nuclear amplitudes (CNI) produce structure in the differential cross sections, allowing one to deduce some information about the Coulomb and nuclear matrix elements. These data were analyzed using an implicit folding procedure [2] to determine the ratio of the nuclear to charge deformation lengths and, hence, the neutron to proton multipole transition matrix elements, M_n/M_p. The inappropriateness of the implicit folding procedure has been discussed elsewhere [3]. Wang and Rapaport [4] determined the isospin nature of the transitions by a comparison of inelastic proton and neutron scattering. The M_n/M_p ratios reported from the alpha scattering [1] were significantly larger than those reported from the comparison of proton and neutron scattering [4].

In an attempt to resolve the large discrepancies in the reported M_n/M_p ratios for the transitions to the first 2_1^+ and 3_1^- states, Horen *et al.* measured the elastic and inelastic scattering of 70 MeV ^{6}Li ions by the even isotopes of zirconium [5,6]. The data were analyzed using a deformed optical model potential (DOMP) [7] to determine a hadronic deformation length δ_l^N. The M_n/M_p ratios deduced in this manner were considerably smaller ($\frac{1}{2}$–$\frac{1}{3}$ times) than those reported from the alpha scattering [1] and were in much better agreement with those reported from the proton-neutron scattering [4]. The ^{6}Li results also support the predictions of a random-phase approximation (RPA) nuclear structure calculation. A partial reanalysis of the alpha-scattering data was performed in which the nuclear deformation parameters reported in [1] were used in a simple schematic relation [see Eq. (16), below] [6]. The resulting M_n/M_p ratios were much smaller than the values reported in [1], but were still significantly larger than those deduced from the ^{6}Li scattering.

In an effort to determine whether the remaining discrepancy was caused by inconsistencies in the data or by the interpretation of the DOMP model result, we undertook an independent measurement of the 35.4 MeV alpha scattering. In order to be able to make direct comparisons with the previous results from alpha scattering, we also analyzed our data using the DOMP.

The data were also analyzed using a folding model in conjunction with the same RPA transition densities used in [6]. In addition, calculations were made using transition densities of the Bohr-Mottelson standard collective model form [8]. This allowed us to investigate the sensitivity of the extracted δ_l^N and $B(El)\uparrow$ to the shape adopted for the transition densities as well as differences in the optical potentials for the entrance and exit channels.

II. EXPERIMENT

Measurements of the scattering of 35.4 MeV alpha particles by $\sim$ 1.0 mg/cm^2, self-supporting targets of ^{90,92,94,96}Zr were performed at the A.W. Wright Nuclear

Structure Laboratory at Yale University. The beam was produced in the ESTU-1 tandem van de Graaf accelerator. The scattered particles were momentum analyzed using an Enge split-pole spectrometer and detected with a two-wire, hybrid ionization counter. An overall energy resolution of ~ 130 keV was obtained. The 2_1^+ and 3_1^- states of ^{96}Zr are just resolved at this resolution.

Elastic cross sections were measured over an angle range of $\theta_{\rm lab} = 6.0°–46.5°$, and inelastic cross sections were measured over an angle range of $\theta_{\rm lab} = 8.0°–46.5°$. For each spectrometer setting, a five-slit plate was inserted before the spectrometer entrance to define the geometry of the measurement [9]. The scattering yield from each of the four zirconium targets was then recorded before moving the spectrometer and the five-slit plate. For angles smaller than $\theta_{\rm lab} = 20°$, slit scattering of the elastically scattered alpha particles produced a long tail which prevented measurement of inelastically scattered particles. For these angles, the five-slit plate was used to calibrate the detector in terms of scattering angle at the target, then removed in order to acquire the data which were then analyzed off-line in 0.25° bins. The vertical aperture of the defining slits was restricted so that the true scattering angle within each bin was essentially equal to the in-plane scattering angle (e.g., the true scattering angle differed from the in-plane scattering angle by less than 0.005° at an in-plane scattering angle of 10°).

The isotopic compositions and the thicknesses of the targets are shown in Table I. These targets are the same ones used in the ^{6}Li scattering experiment [6]. A new measurement, via the energy loss of alpha particles, of the thickness of these targets indicated that they are roughly 10% thinner than previously believed. This accounts for the renormalization that was necessary in the analysis of the ^{6}Li scattering cross sections [6]. In addition to the compositions shown in Table I, each of the targets contained small contamination of carbon and oxygen. The ^{96}Zr target also contained a small amount of tungsten. It was necessary to correct the small angle ^{96}Zr elastic scattering for the presence of the tungsten. The main effects of the carbon and oxygen impurities are on the inelastic scattering to the 2_1^+ states in ^{92,94}Zr just below 20°, near the end of the region of CNI. For the other states, the carbon and oxygen elastic scattering crossover occurred well beyond the CNI region.

Absolute cross sections were calculated using the target thickness and compositions, the experimental geometry, and the Faraday cup readings. The data were corrected for the live time of the acquisition system. The resulting elastic scattering cross sections have been measured with an uncertainty of ~ 5%, while the inelastic cross sections have uncertainties of 7–10%.

III. MODELS AND ANALYSIS

The data have been analyzed using a deformed optical model potential (DOMP) as well as a folding model to calculate the scattering cross sections. The transitions have been treated as vibrational excitations of a spherical nucleus. In the folding analysis, the transition densities are taken either to be of the Bohr-Mottelson standard collective model form [8], or are obtained from a random-phase approximation (RPA) nuclear structure calculation [6,10] that predicts the neutron and proton transition densities. The effective interaction was determined by fitting the elastic scattering. The scattering cross sections were calculated using the coupled-channels computer program PTOLEMY [11].

A. Deformed optical model potential analysis

In the DOMP model, we assume that the short range of the nuclear interaction causes the scattering potential to have a shape similar to that of the underlying nuclear density distribution [7]. The deformation length of the DOMP potential is assumed to be the same as that of the deformed nuclear density distribution. While plausible, this assumption can be shown to be inconsistent with folding model calculations and thus makes questionable the meaning of deformation lengths deduced from analyses of inelastic data using the DOMP model [3]. However, we analyze our data with the DOMP model in order to make comparisons with earlier works which have also employed this method [1,6].

1. Elastic scattering

The optical potential used to describe the elastic scattering was taken to be of the standard Woods-Saxon form

$$U(r) = -Vf(x_V) - iWf(x_W) \ , \qquad (1)$$

where

$$f(x_i) = (1 + e^{x_i})^{-1}, \quad x_i = (r - R_i)/a_i \ ,$$

$$R_i = r_i(A_p^{1/3} + A_t^{1/3}) \text{ fm}, \quad i = V, W \ .$$

A_p and A_t are the mass numbers of the projectile and target, respectively. The real and imaginary parts of the potential were taken to have the same shape, i.e., $r_V = r_W$ and $a_V = a_W$. The Coulomb potential was taken to be that of a point charge interacting with a uniform

TABLE I. Thickness and isotopic composition of the zirconium targets.

Target	Thickness (mg/cm^3)	Composition (%) ^{90}Zr	^{91}Zr	^{92}Zr	^{94}Zr	^{96}Zr
^{90}Zr	0.855	97.67	0.96	0.71	0.55	0.13
^{92}Zr	0.845	2.86	1.29	94.57	1.15	0.14
^{94}Zr	0.910	1.67	0.42	0.76	96.93	0.22
^{96}Zr	0.828	7.25	1.41	2.24	3.85	85.25

TABLE II. Woods-Saxon optical model parameters determined from fit to elastic scattering data. A Coulomb radius parameter of r_c = 1.20 fm was fixed for all cases.

Isotope	V (MeV)	W (MeV)	r_u (fm)	a_u (fm)	χ^2/pt
^{90}Zr	220.59	23.989	1.018	0.575	0.880
^{92}Zr	241.51	41.145	0.993	0.600	0.596
^{94}Zr	253.61	74.592	0.959	0.645	0.776
^{96}Zr	279.42	86.879	0.953	0.645	1.271

charge distribution of radius $R_c = r_c(A_p^{1/3} + A_t^{1/3})$ fm. In this work we adopt the value $r_c = 1.2$ fm.

The program PTOLEMY was used to optimize the fit to the elastic data from each target by varying the four optical model parameters using the standard χ^2 criterion and the experimental uncertainties. The optical model parameters thus obtained are shown in Table II. There is considerable ambiguity associated with optical model parameters determined from fits to low energy alpha-particle scattering, although it is known that those giving equivalent fits to the elastic data also yield very similar inelastic cross sections [1]. We have chosen sets with V between 200 and 300 MeV. The optical model parameters listed in Table II were used in the DOMP calculations of the alpha inelastic scattering. The corresponding fits to the elastic data are shown in Fig. 1.

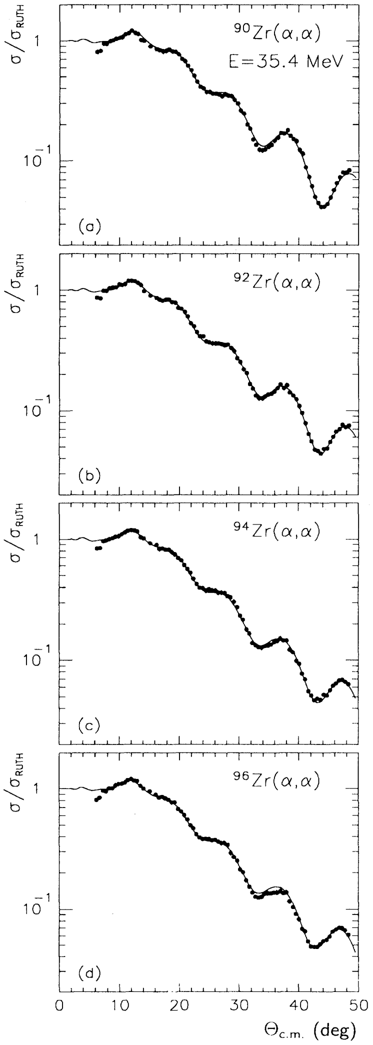

FIG. 1. Optical model fits to the elastic scattering data for ^{90,92,94,96}Zr+α at $E_{\rm lab}$ = 35.4 MeV. The optical model parameters are given in Table II. The cross sections are plotted relative to the Rutherford cross section.

2. Inelastic scattering

In the DOMP calculations [6,7,11], the nuclear transition potential for angular momentum transfer l is assumed to have the form

$$H_l^N(r) = -\delta_l^N \frac{dU(r)}{dr} , \qquad (2)$$

where $U(r)$ is the optical potential, Eq. (1), with parameters determined by the fits to the elastic data. Here we have assumed that the real and imaginary deformation lengths δ_l^N are equal. The total transition potential is the sum of the nuclear and Coulomb transition potentials. At large radii, the Coulomb interaction is completely determined by the reduced electric transition probability, $B(El)\uparrow$. For radii less than R_c, the potential was taken to have the form for a point charge interacting with a deformed, uniformly charged sphere of radius R_c [11,12]:

$$H_l^C(r) = \frac{4\pi Z_p e}{2l+1}[B(El)\uparrow]^{1/2}\begin{cases} 1/r^{l+1}, & r > R_c \\ r^l/R_c^{2l+1}, & r \le R_c \end{cases} \qquad (3)$$

where Z_p is the atomic number of the projectile. The reduced electric transition probability is given in terms of the proton multipole transition matrix element M_p as

$$B(El)\uparrow = e^2 M_p^2 = e^2 \left| \int g_l^p(r) r^{l+2} dr \right|^2 , \qquad (4)$$

where $g_l^p(r)$ is the proton transition density, and M_p is the proton 2^l-pole moment. The neutron multipole transition matrix element M_n is given similarly, with $g_l^p(r)$ replaced by $g_l^n(r)$ [12].

The mass (isoscalar) multipole transition matrix element is defined as $M_{\rm IS} = M_n + M_p$, and the reduced mass transition probability is given in analogy with that for electric transitions as

$$B_{\rm IS}(l) = |M_n + M_p|^2 . \qquad (5)$$

From Eqs. (4) and (5), the magnitude of the ratio of neutron to proton multipole matrix elements is given by

$$|M_n/M_p| = \left| \frac{B_{\mathrm{IS}}(l)}{B(El)\uparrow/e^2} \right|^{1/2} - 1 \; . \qquad (6)$$

This ratio is an indication of the isospin nature of the transition; for a simple mass oscillation it would have the value N/Z.

As is often done, we assume that the neutron and proton transition densities have the same radial shape, $g(r)$, i.e.,

$$g_l^n(r) = \frac{N}{A}\delta_l^n g(r), \quad g_l^p(r) = \frac{Z}{A}\delta_l^p g(r) \; , \qquad (7)$$

where N, Z, and A are the target neutron, proton, and mass number, respectively. A typical choice for $g(r)$ is the standard Bohr-Mottelson collective form [8],

$$g(r) = -\frac{d\rho(r)}{dr} \; , \qquad (8)$$

where $\rho(r)$ is the ground state density distribution.

An isoscalar (or mass) deformation length may be defined as

$$A\delta_l^{\mathrm{IS}} = (N\delta_l^n + Z\delta_l^p) \; . \qquad (9)$$

As the projectile is an isoscalar probe, we make the additional assumption that the deformation length of the potential in the DOMP model, Eq. (2), is the same as the mass deformation length, i.e., $\delta_l^N = \delta_l^{\mathrm{IS}}$. A measure of the proton deformation length can be obtained from the $B(El)\uparrow$ value by using the standard expression for a uniform charge distribution of radius $R_c = 1.2A_T^{1/3}$ fm,

$$B(El)\uparrow = (\delta_l^p)^2 \left[\frac{3ZeR_c^{l-1}}{4\pi}\right]^2 \; . \qquad (10)$$

This expression corresponds to the proton radial transition density being a delta function at $r = R_c$, but calculations with a more realistic shape indicate that the error made with this expression is small, e.g., less than 5% in δ_l^p.

The inelastic cross sections were calculated using coupled channels [7,11]. The effects of the couplings of the inelastic channels on the elastic cross sections were found to be small, so the optical model parameters deduced from fitting the elastic data were adequate for use in the calculations of the inelastic cross sections. We performed a series of calculations by gridding on $B(El)\uparrow$ and δ_l^N to obtain the best fits to the inelastic data.

a. 2^+ states. In Fig. 2, the best fit calculations for exciting the 2_1^+ states are compared with the data. The corresponding $B(E2)\uparrow$ and δ_2^N are listed in Table III, where they are compared with the results of Rychel *et al.* [1]. The overall agreement between these two alpha-particle measurements is considered to be excellent. Rychel *et al.* [1] analyzed their data by means of χ^2 fitting, whereas we have used a more visual means. In their χ^2 analysis, Rychel *et al.* [1] restricted their analysis to data for which $\theta_{\mathrm{c.m.}} < 30^\circ$ because they found that inclusion of the larger angle data broadened their χ^2 distributions. The reason for this can most likely be understood from Fig. 2, where it is clear that at the larger angles there are significant phase shifts in the oscillations of the angular distributions between the data and the calculated curves. The maxima for the calculations of the ^{90}Zr cross sections occur at smaller angles than the data, while the maxima for the calculations of the other zirconium isotopes occur at larger angles than the data. Because no experimental parameters other than the target were changed between experimental runs (e.g., spectrometer angle, position of the five-slit plate, etc.), we believe this effect to be real, and not an artifact of some systematic error in the experiment. Furthermore, our data are in excellent agreement with the independent measurement of Rychel *et al.* [1]. We address the possible explanations for this shift of phase between the data and calculations in a later section.

In the top section of Fig. 3 we show calculations for excitation of the 2_1^+ state of ^{90}Zr by pure Coulomb, pure nuclear, and combined interactions. The cross section at the larger angles is dominated by the nuclear component which determines δ_l^N. There is a strong interference near

TABLE III. Comparison of δ_l^N and $B(El)\uparrow$ deduced from DOMP analyses of the 35.4 MeV (α,α') data of Rychel *et al.* and the present work. For the 3_1^- states, we give a range of values for $B(El)\uparrow$ which is supported by the data (see text). The values from Rychel *et al.* [1] were derived using the table and formulas therein. Also listed are δ_l^N deduced from the 70 MeV ^{6}Li scattering of Horen *et al.* [5,6], and the adopted $B(El)\uparrow$ used in the DOMP analysis.

	Rychel *et al.*		Present work		Horen *et al.*	
Nucleus	δ_l^N (fm)	$B(El)\uparrow$ (e^2b^l)	δ_l^N (fm)	$B(El)\uparrow$ (e^2b^l)	δ_l^N (fm)	$B(El)\uparrow$[a] (e^2b^l)
2_1^+ states						
^{90}Zr	0.408±0.016	0.062±0.006	0.400±0.020	0.063±0.005	0.396	0.063±0.005
^{92}Zr	0.731±0.007	0.069±0.006	0.673±0.034	0.075±0.010	0.557	0.083±0.006
^{94}Zr	0.633±0.006	0.050±0.005	0.632±0.032	0.058±0.010	0.525	0.066±0.014
^{96}Zr	0.639±0.003	0.027±0.007	0.589±0.030	0.025±0.005	0.466	0.055±0.022
3_1^- states						
^{90}Zr	0.806±0.007	0.0664±0.0073	0.750±0.038	0.051−0.091	0.686	0.071
^{92}Zr	0.894±0.005	0.0556±0.0077	0.831±0.042	0.047−0.087	0.742	0.067
^{94}Zr	1.020±0.006	0.0794±0.0118	0.932±0.047	0.067−0.107	0.839	0.087
^{96}Zr	1.228±0.011	0.104±0.011	1.111±0.056	0.060−0.180	1.051	0.120

[a] The $B(El)\uparrow$ were fixed in the analysis of the ^{6}Li scattering data [5,6].

$\theta \approx 15°$ which can be used to determine the ratio of the nuclear to Coulomb amplitudes, i.e., δ_l^N/δ_l^p. In the analysis of the present data as well as that of Rychel *et al.* [1], emphasis was placed upon reproducing the shape and magnitude of the data in the smaller angle regions. The fact that the calculations also match the peak cross sections in magnitude at the larger angles suggests that other phenomena are occurring which affect the relative phase between the measured and calculated oscillations. We have investigated the inclusion of other couplings as well as reorientation effects, but these did not produce phase shifts of the observed magnitudes.

In Table III we also list the δ_2^N obtained from DOMP analyses of the ^{6}Li data [6] in which the values of $B(E2)\uparrow$ were held fixed. As noted earlier [6], there is excellent agreement between the alpha-particle and ^{6}Li results for the 2_1^+ state of ^{90}Zr. The agreement for ^{92,94}Zr is not quite as good, as the mean values of the δ_2^N deduced from the alpha-scattering data are about 20% larger than those from the ^{6}Li measurements for these two isotopes. Part of this could be accounted for by the small differences in the corresponding $B(E2)\uparrow$ values, but it does not appear that this would be sufficient to completely account for all of the differences. In light of the excellent agreement found for the 2_1^+ state of ^{90}Zr, the reason for the differences obtained for the δ_2^N for ^{92,94}Zr is not clear. Although it has been commonly expected that the δ_l^N extracted from inelastic data for different probes using a DOMP analysis would be nearly the same, there is no guarantee that the deficiencies in the DOMP method [3] will apply equally to different probes. The fact that the deduced δ_2^N agree for the 2_1^+ state of ^{90}Zr but differ for the 2_1^+ states of ^{92,94}Zr might be a reflection of nuclear structure differences in the transition densities that are sampled somewhat differently by the two probes. Our $B(E2)\uparrow = 0.058 \pm 0.010 e^2b^2$ for the 2_1^+ state of ^{94}Zr is in excellent agreement with a recently measured [13] value of $0.060 \pm 0.004 e^2b^2$. For the 2_1^+ state of ^{96}Zr, the $B(E2)\uparrow$ from the DOMP analyses of the alpha-particle scattering are about one-half the adopted value [14], but essentially overlap within experimental uncertainties. Comparison between the alpha-particle and ^{6}Li results for this state of ^{96}Zr is difficult because of the poor experimental resolution achieved in the ^{6}Li measurements [5,6].

b. 3^- states. Unlike the 2_1^+ states, the Coulomb scattering amplitude contributes very little to the 3_1^- inelastic scattering cross sections. This is illustrated in Fig. 3. The Coulomb contribution to the 2_1^+ cross section is significant even at the larger angles, but has only a small effect on the 3_1^- cross section. Fits to the 3_1^- data therefore measure the nuclear deformation parameter δ_3^N, essentially independent of the adopted value for $B(E3)\uparrow$. Ac-

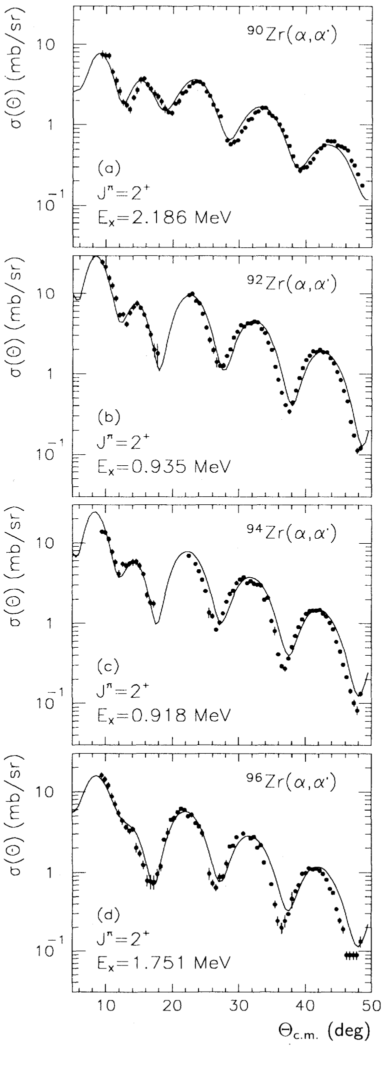

FIG. 2. Differential cross sections for exciting the 2_1^+ states of ^{90,92,94,96}Zr. The curves are the coupled channels calculations of the cross sections using the DOMP.

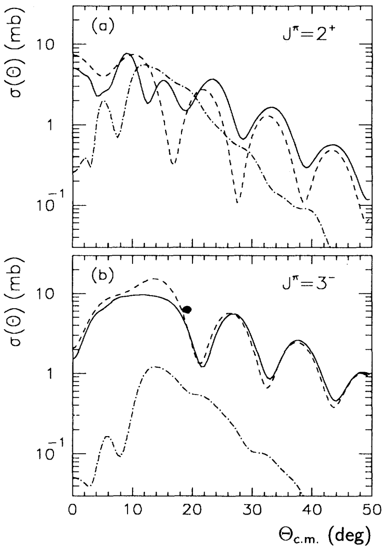

FIG. 3. Contributions of the Coulomb and nuclear interactions to the total cross sections for (a) the 2_1^+ state and (b) the 3_1^- state of ^{90}Zr. The curves are calculated in the framework of the DOMP. In (a), the calculations use $B(E2)\uparrow = 0.063 e^2b^2$ and $M_n/M_p = 0.84$. In (b), the calculations use $B(E3)\uparrow = 0.071 e^2b^3$ and $M_n/M_p = 0.75$. The dashed curve corresponds to the cross section arising from the nuclear potential only, the dot-dashed curve to the Coulomb potential only, and the solid curve to the total cross section.

curate independent measurements of $B(E3)\uparrow$ are therefore necessary to deduce the value of M_n/M_p for these states. Unfortunately, except for ^{96}Zr [15], the values of $B(E3)\uparrow$ for the zirconium isotopes are only poorly known.

In order to determine δ_3^N from our data, we fixed $B(E3)\uparrow$ to the values adopted for the ^{6}Li analysis [5,6]. These values are shown in the last column of Table III, while our deduced values for δ_3^N are given in the fourth column. Using our deduced δ_3^N, we then performed calculations for several values of $B(E3)\uparrow$. In the fifth column of Table III, we list the upper and lower values of $B(E3)\uparrow$ which are supported by our data.

In Fig. 4 we show the results of calculations in which we use our deduced δ_3^N and the values of $B(E3)\uparrow$ adopted in [6]. For ^{96}Zr, we show a calculation using the value $B(E3)\uparrow= 0.120e^2b^3$ (solid curve) used in [6], as well as a calculation using the recently determined [15] value $B(E3)\uparrow= 0.180 \pm 0.018e^2b^3$ (dashed curve). These two curves are almost indistinguishable, except in the region $10^\circ \lesssim \theta_{\text{c.m.}} \lesssim 15^\circ$, even though the values of $B(E3)\uparrow$ used to make the calculations are considerably different. This illustrates the insensitivity of using the alpha-particle scattering data to determine $B(E3)\uparrow$ values for these zirconium isotopes.

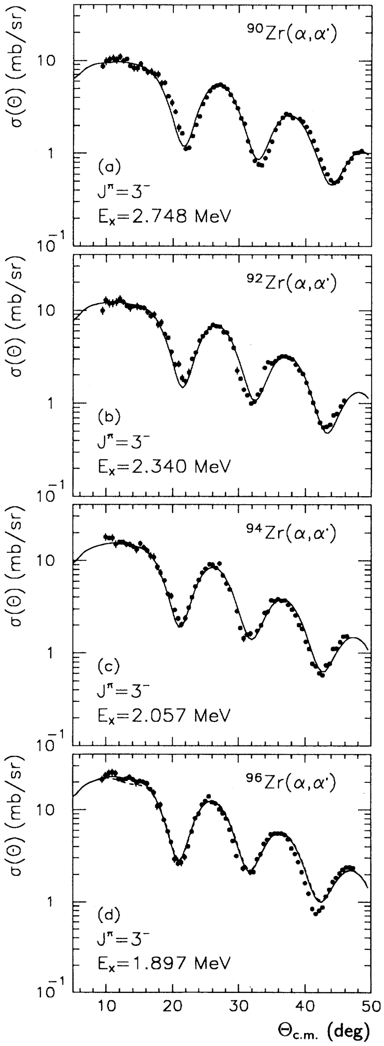

FIG. 4. Differential cross sections for exciting the 3_1^- states of ^{90,92,94,96}Zr. The curves are the coupled channels calculations of the cross sections using the DOMP. For ^{96}Zr, the solid curve was calculated using $B(E3)\uparrow= 0.120e^2b^3$, while the dashed curve was calculated using $B(E3)\uparrow= 0.180e^2b^3$.

B. Folding model analysis

A complex alpha-nucleon effective interaction having a Gaussian form [12,16] was used in the folding model analyses. The parameters were deduced from fits to the elastic data.

1. Elastic scattering

The optical potential is obtained by folding the effective alpha-nucleon interaction $\nu(r_{1\alpha})$ over the ground state density distribution of the target nucleus [7,12]:

$$U_F(r) = \int \rho_A(r_1)\nu(r_{1\alpha})d\mathbf{r}_1 \ , \qquad (11)$$

where $r_{1\alpha} = |\mathbf{r} - \mathbf{r}_1|$. The real and imaginary parts of $\nu(r)$ were assumed to have the same shape.

The effective interaction is taken to have a Gaussian form,

$$\nu(r) = -(V + iW)\exp(-r^2/t^2) \ , \qquad (12)$$

where V, W, and t are to be determined from fits to the elastic data.

A two-parameter Fermi shape was used for the ground state density distributions of the zirconium isotopes

$$\rho(r) = \rho_0(1 + e^x)^{-1}, \quad x = (r - c)/a \ . \qquad (13)$$

Initially, the diffuseness parameter a for each of the zirconium isotopes was set to the same value and the radius was scaled by $A^{1/3}$. Folded potentials were calculated for a variety of ranges t of the alpha-nucleon interaction and least square fits to the data were made using the program PTOLEMY. It was found that the minimum χ^2 occurred at a different range for each isotope, and the values of V and W varied considerably. Based upon the increase in the range as a function of A at the minimum χ^2, we decided to investigate whether we could find a single effective interaction which would simultaneously fit the elastic data for each of the isotopes. To this end, we scaled the radius of the ground state density as $A^{1/3}$ and gridded on the diffuseness while fixing the range of the effective interaction at $t = 1.94$ fm, a value used successfully in earlier works to describe alpha scattering [12,16]. The searches with folded potentials under these conditions resulted in the values of the diffuseness parameters tabulated in Table IV and the strengths of the potentials given in Table V. The corresponding fits to the elastic cross sections are shown in Fig. 5.

As seen in Table V, the depths of the real part V of the

TABLE IV. Parameters[a] for a two-parameter Fermi model of the ground state density distributions of the zirconium isotopes, where $\rho(r) = \rho_0(1 + e^{(r-c)/a})^{-1}$.

Isotope	c (fm)	a (fm)	RMS radius (fm)
^{90}Zr	4.90	0.519	4.258
^{92}Zr	4.94	0.529	4.302
^{94}Zr	4.97	0.539	4.340
^{96}Zr	5.01	0.549	4.385

[a] Slightly different parameters for the ground state density distribution were used in Refs. [5,6].

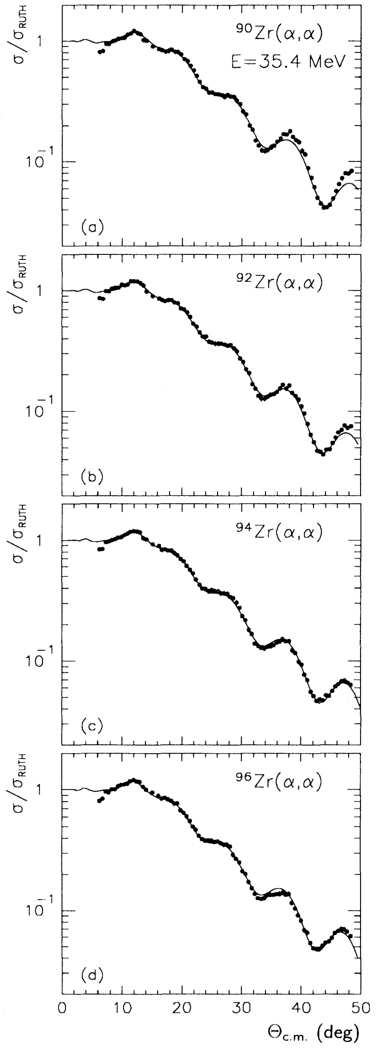

FIG. 5. Folding model fits to the elastic scattering cross sections for ^{90,92,94,96}Zr+α at $E_{\mathrm{lab}} = 35.4$ MeV, using an effective alpha-nucleon interaction and Fermi density distributions. The cross sections are plotted relative to the Rutherford cross section. The parameters of the ground state density distributions are given in Table IV, while the strengths of the interaction are given in Table V.

TABLE V. Strengths of the real and imaginary parts of the alpha-nucleon effective interaction which fit the elastic alpha scattering from the zirconium isotopes.

Isotope	V (MeV)	W (MeV)	χ^2/pt
^{90}Zr	49.736	16.774	2.930
^{92}Zr	48.443	18.153	1.294
^{94}Zr	48.263	18.081	0.841
^{96}Zr	47.348	18.977	1.394

effective interaction are consistent to within 5% and the depths of the imaginary part W to within 13%. The diffuseness parameter is seen to increase monotonically from ^{90}Zr to ^{96}Zr. There do not exist nuclear structure calculations of the ground state densities of these zirconium isotopes with which to compare this trend. The noted differences in the depths of the effective interaction would not change the calculated cross sections significantly.

2. Inelastic scattering

The transition potentials for inelastic scattering were calculated using the generalization of Eq. (11) in which the ground state density distributions are replaced by the transition densities [12,16]. We performed analyses using transition densities obtained from a quasiparticle random-phase approximation (RPA) calculation, as well as transition densities having the standard collective model Bohr-Mottelson (BM) form of Eq. (8).

a. RPA transition densities. In order to examine the consistency of folding model calculations for alpha-particle and ^{6}Li particle scattering, transition densities which were obtained from quasiparticle RPA calculations using separable quadrupole or octupole interactions were used in folding model calculations. The RPA calculations are described in [6,10]. The corresponding $B(El)\uparrow$ and

TABLE VI. Summary of the predictions of the RPA calculations. The RPA calculations were constrained to reproduce the $B(El)\uparrow$ values of column 3.

			RPA calculation[a]		
Isotope	E_x (MeV)	$B(El)\uparrow$ (e^2b^l)	E_x (MeV)	M_p (e fm^l)	M_n/M_p
2_1^+ states					
^{90}Zr	2.186	0.063[b]	2.51	25.1	0.84
^{92}Zr	0.935	0.083[b]	1.40	28.9	1.49
^{94}Zr	0.918	0.066[b,c]	1.55	25.9	1.69
^{96}Zr	1.751	0.055[b]	2.02	23.3	1.66
3_1^- states					
^{90}Zr	2.748	0.071[d]	2.73	267	0.75
^{92}Zr	2.340	0.067[d]	2.64	257	0.87
^{94}Zr	2.057	0.087[d]	2.35	295	1.06
^{96}Zr	1.897	0.120[e]	1.96	346	1.22

[a] References [6,10].

[b] Reference [14].

[c] A recent remeasurement [13] found $B(E2)\uparrow = 0.060 \pm 0.004e^2b^2$.

[d] Reference [17].

[e] References [5,6]; a recent remeasurement [15] found $B(E3)\uparrow = 0.180 \pm 0.018e^2b^3$.

M_n/M_p were taken from Table III of [6], and are reproduced in Table VI. In Fig. 6 the results of the folding model calculations for the 2_1^+ states (solid curves) are compared with the data. Except for the strong interference region for the 2_1^+ state of ^{96}Zr, the folding model calculations with RPA transition densities reproduce the alpha-particle data in a manner comparable to the folding model calculations for the ^{6}Li scattering.

Similar calculations for the 3_1^- states (solid curves) are compared with the data in Fig. 7. Again we find that the results of the folding calculations for the alpha-particle scattering are similar to those for the ^{6}Li scattering. For both projectiles, the calculations significantly underestimate the data.

The folding calculations using the RPA transition densities reproduce the magnitudes of the 2_1^+ cross sections at the larger angles which suggests that the sum of the neutron and proton matrix elements, or the isoscalar (or mass) matrix element, is reasonable. However, except for ^{90}Zr, the calculations fail to reproduce the CNI region accurately; this is especially noticeable for ^{96}Zr. This indicates that the predicted ratios of M_n/M_p from the RPA calculations are not correct.

Finally, we call attention to the phase shifts between the oscillations in the calculated and measured angular distributions which are similar to those observed in the DOMP calculations.

b. Bohr-Mottelson transition densities. In the standard collective model, deformations are introduced by making the position of the nuclear surface dependent on

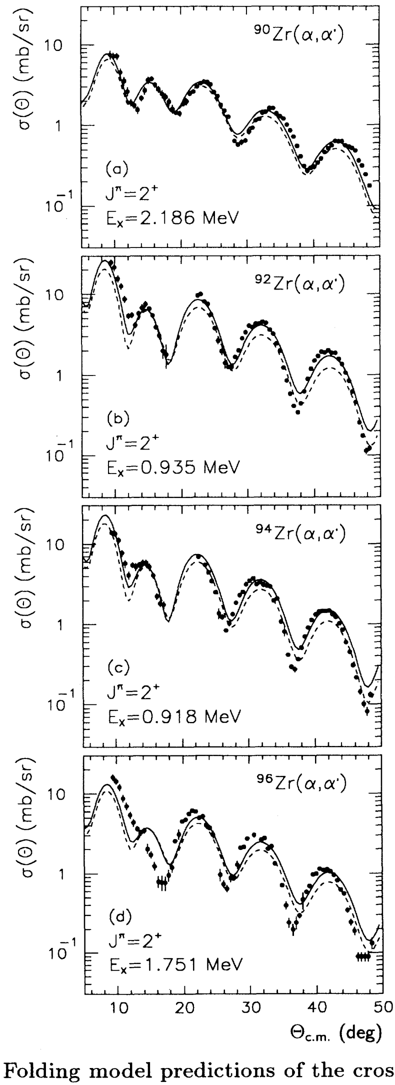

FIG. 6. Folding model predictions of the cross sections for exciting the 2_1^+ states of ^{90,92,94,96}Zr using the $B(E2)\uparrow$ values and M_n/M_p ratios predicted by the RPA, as given in Table VI. The solid curves were calculated using the RPA transition densities, while the dashed curves were calculated using BM transition densities constrained to yield the same $B(E2)\uparrow$ and M_n/M_p of the RPA structure calculations.

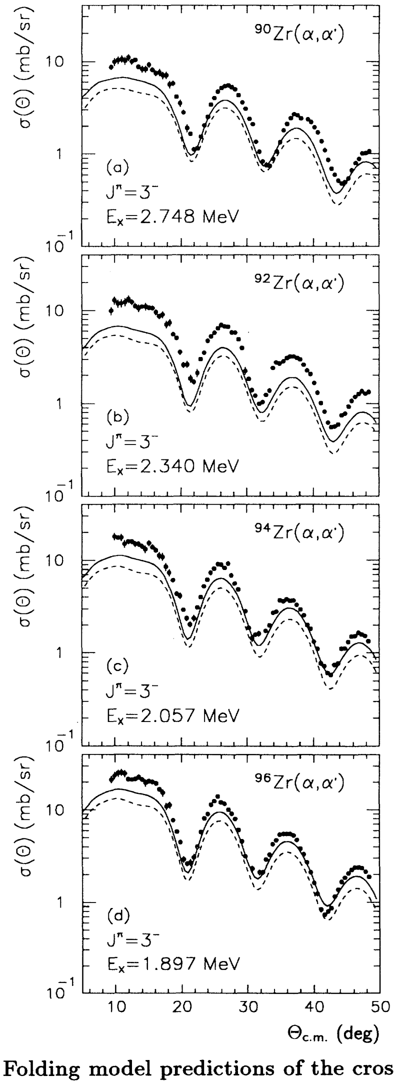

FIG. 7. Folding model predictions of the cross sections for exciting the 3_1^- states of ^{90,92,94,96}Zr using the $B(E3)\uparrow$ values and M_n/M_p ratios predicted by the RPA, as given in Table VI. The solid curves were calculated using the RPA transition densities; the dashed curves were calculated using BM transition densities constrained to yield the same $B(E3)\uparrow$ and M_n/M_p of the RPA structure calculations.

the direction of **r** in the usual manner [7,12],

$$R(\theta,\phi) = R\left(1+\sum_{\lambda\mu}\alpha_{\lambda\mu}Y_\lambda^\mu(\theta,\phi)^*\right) . \quad (14)$$

The $\alpha_{\lambda\mu}$ are operators which create or annihilate one phonon with angular momentum λ and z-projection μ. The transition densities are now obtained by making a Taylor series expansion for $\rho(r)$ [7]. The resulting densities to be used in the folding integral for the transition potential are then given by

$$g_l(r) = -\delta_l^M \frac{d\rho(r)}{dr} , \quad (15)$$

where $\rho(r)$ is the ground state density distribution [Eq. (13)], and δ_l^M is the mass deformation length. Hence, the deformation parameters deduced using the folding model are the deformations of the density distributions of the target nuclei themselves. In the DOMP, it was assumed that the measured deformations of the potentials were equal to the deformations of the underlying nuclear density distributions. While the form for the density distributions must be adopted from some model, measurement of the inelastic scattering gives some measure of the properties of this distribution.

(i) Calculated cross sections using the RPA transition densities. Folding model calculations were performed using BM transition densities which gave the same values for $B(El)\uparrow$ and M_n/M_p as were used in the RPA calculations above. The results of these calculations are shown as dashed curves in Fig. 6 for the 2_1^+ states and Fig. 7 for the 3_1^- states. The calculated cross sections using the BM transition densities are systematically lower than those using RPA transition densities. The reasons for this can be seen in Figs. 8–13, where the BM and RPA transition densities and potentials are compared. The tails of the RPA transition potentials are seen in Figs. 9 and 11 to be larger than those of the BM transition potentials in the region over which the interaction takes place, i.e., $7 \lesssim r \lesssim 11$ fm. This is more clearly seen in Figs. 12 and 13, where the ratio of the BM transition potentials to the RPA transition potentials is plotted. In order to produce cross sections of the same magnitude as the RPA densities, the BM densities will require larger deformations δ_l^M, and therefore lead to larger extracted M_n/M_p ratios. Thus we see that the extracted M_n/M_p ratios are fairly sensitive to the assumed shapes for the transition densities.

Also shown in Figs. 9 and 11 are the transition potentials corresponding to the DOMP fits to the 2_1^+ and 3_1^- states, respectively.

(ii) Cross section fits with Bohr-Mottelson transition densities. Because PTOLEMY does not have a search routine for inelastic scattering, folding model calculations of the inelastic cross sections were performed by gridding on the values of δ_l^N and $B(El)\uparrow$ assuming BM transition densities. Calculated cross sections using best fit values of δ_2^N and $B(E2)\uparrow$ are compared with the data in Fig. 14. Although the calculations reproduce the small angle data and the magnitude of the large angle data, phase shifts can be seen analogous to those found in the

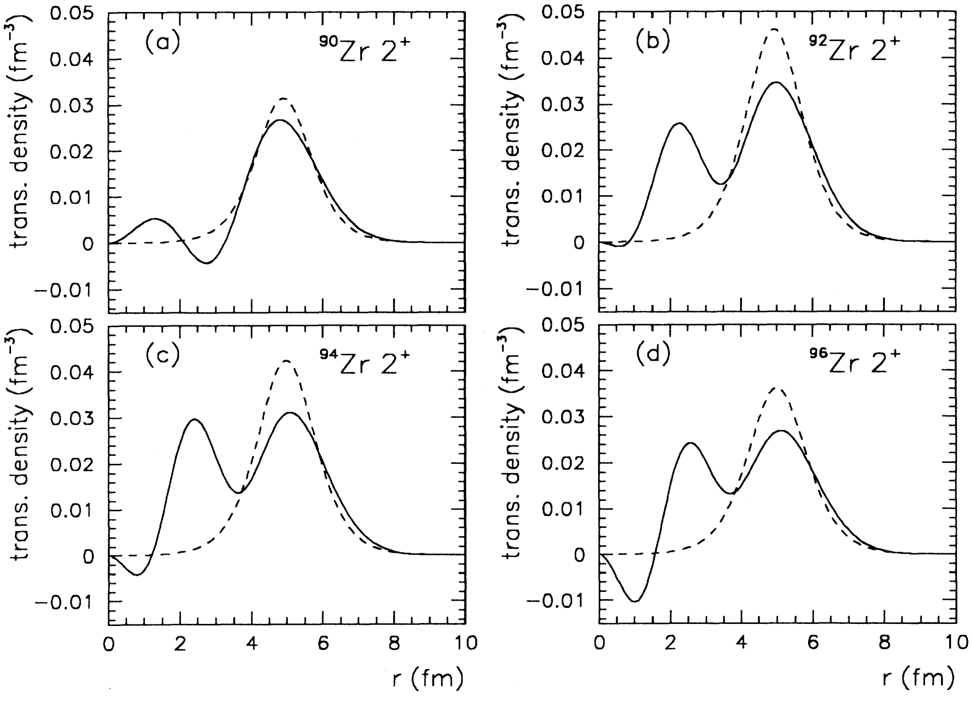

FIG. 8. Comparison of the RPA and BM transition densities for the excitation of the 2_1^+ states of ^{90,92,94,96}Zr which were used to calculate the curves of Fig. 6. The solid curves are the RPA transition densities, while the dashed curves are the BM transition densities. These transition densities produce the $B(E2)\uparrow$ values and M_n/M_p ratios predicted by the RPA calculation as given in Table VI.

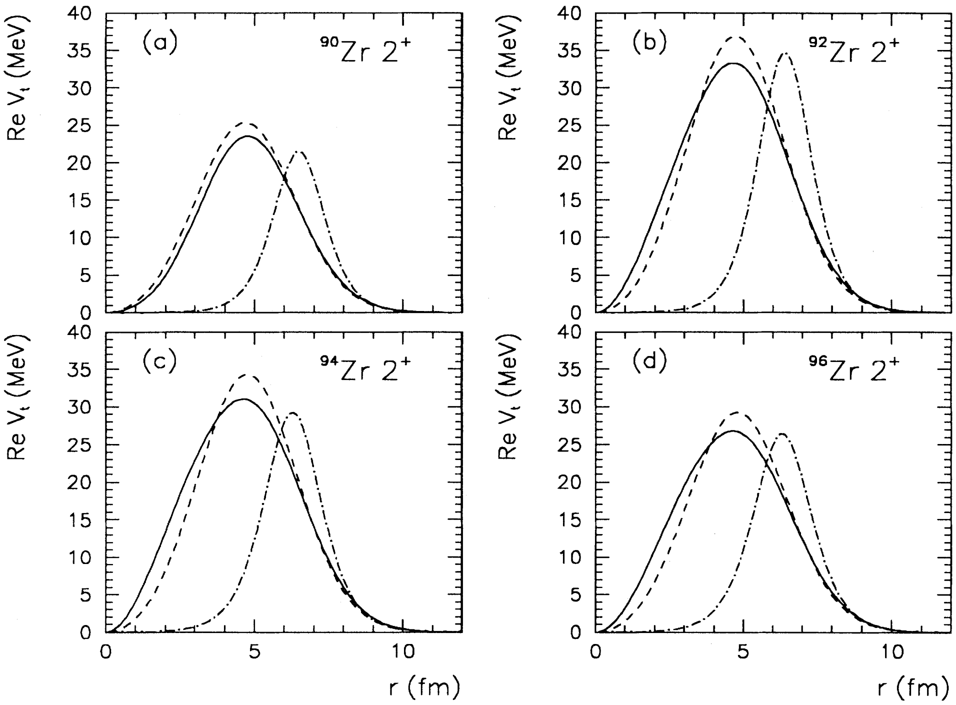

FIG. 9. Comparison of the transition potentials for the excitation of the 2_1^+ states of ^{90,92,94,96}Zr, obtained by folding the effective alpha-nucleon interaction with the transition densities of Fig. 8. The RPA transition potentials are shown as solid curves, while the BM transition potentials are shown as dashed curves. Also shown as dash-dot curves are the DOMP transition potentials.

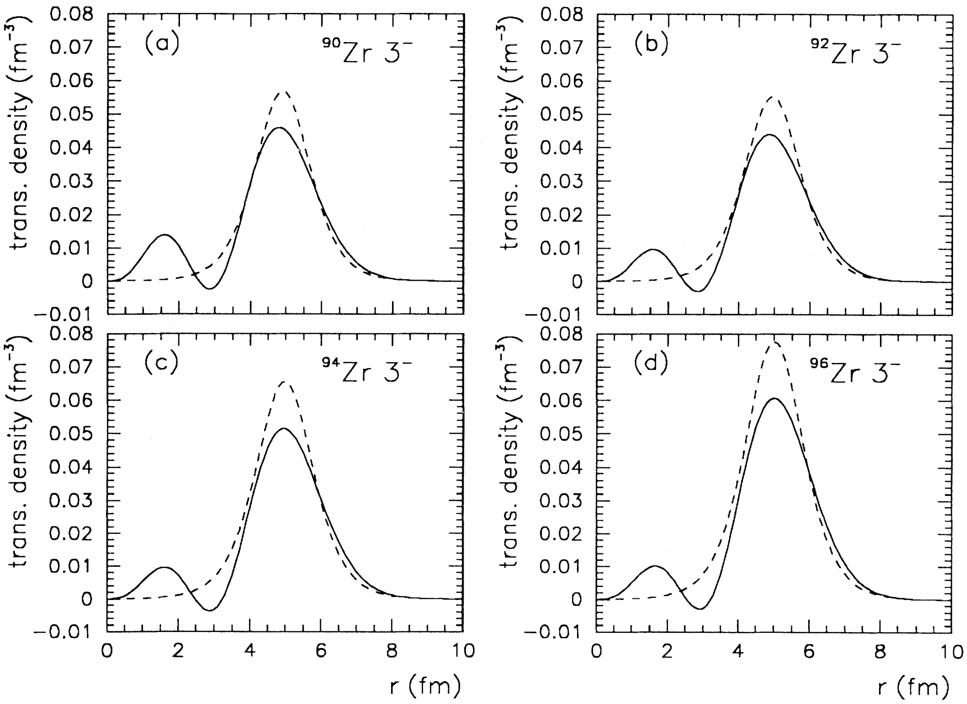

FIG. 10. Comparison of the RPA and BM transition densities for the excitation of the 3_1^- states of ^{90,92,94,96}Zr which were used to calculate the curves of Fig. 7. The solid curves are the RPA transition densities, while the dashed curves are the BM transition densities. These transition densities produce the $B(E3)\uparrow$ values and M_n/M_p ratios predicted by the RPA calculation as given in Table VI.

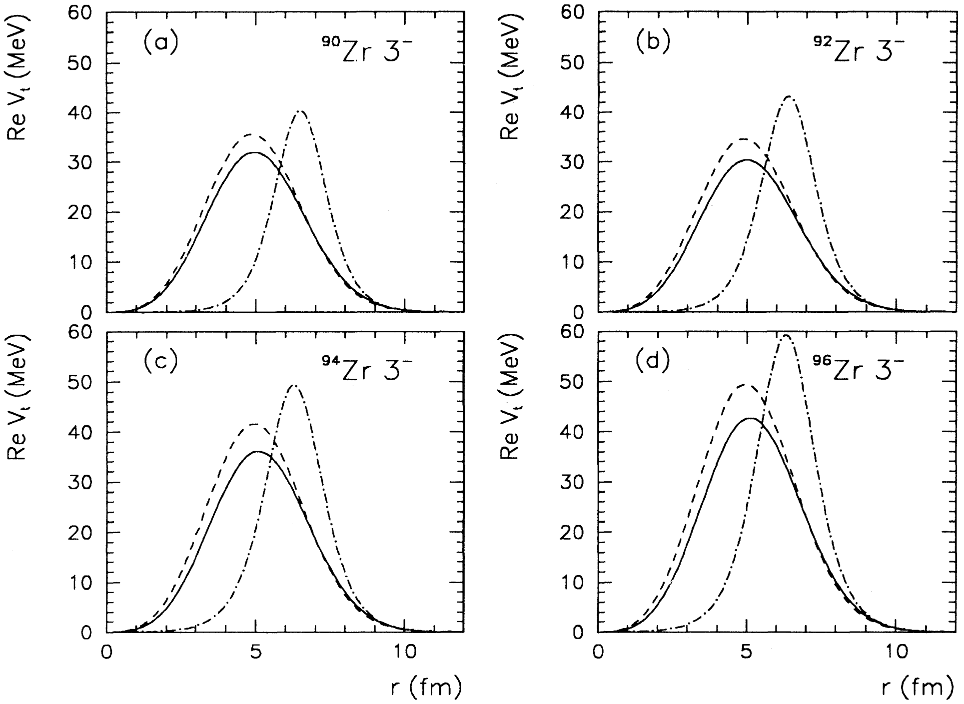

FIG. 11. Comparison of the transition potentials for the excitation of the 3_1^- states of ^{90,92,94,96}Zr, obtained by folding the effective alpha-nucleon interaction with the transition densities of Fig. 10. The RPA transition potentials are shown as solid curves, while the BM transition potentials are shown as dashed curves. Also shown as dash-dot curves are the DOMP transition potentials.

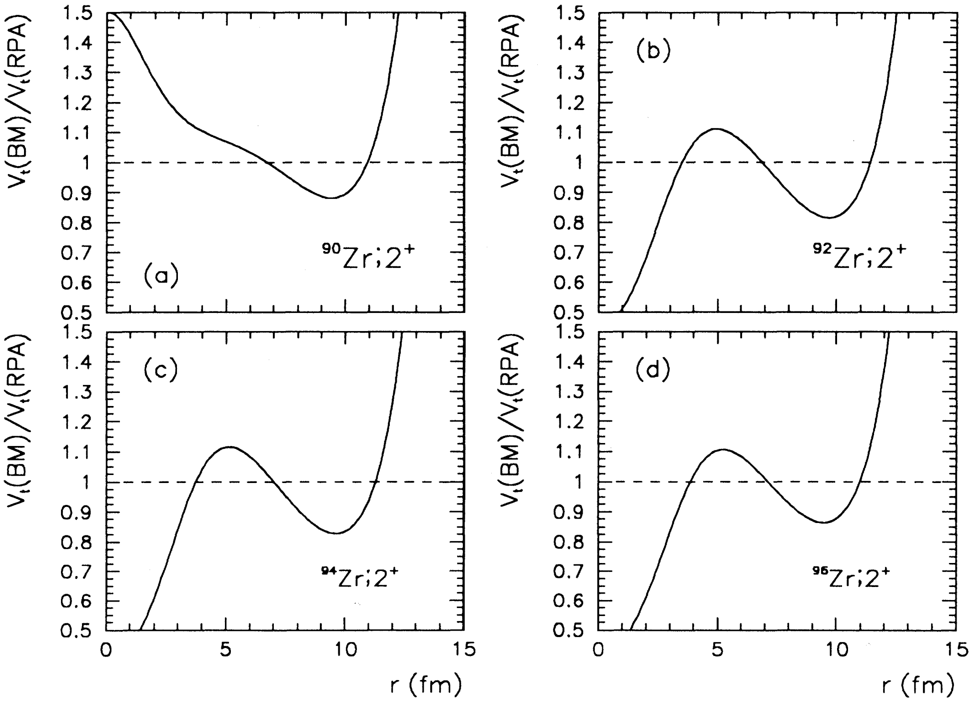

FIG. 12. Ratio of the real part of the BM to RPA transition potentials for exciting the 2_1^+ states of ^{90,92,94,96}Zr. Note that the BM transition potential is smaller than the RPA transition potential for 7 fm$\lesssim r \lesssim$ 11 fm, the dominant region where the scattering interaction takes place.

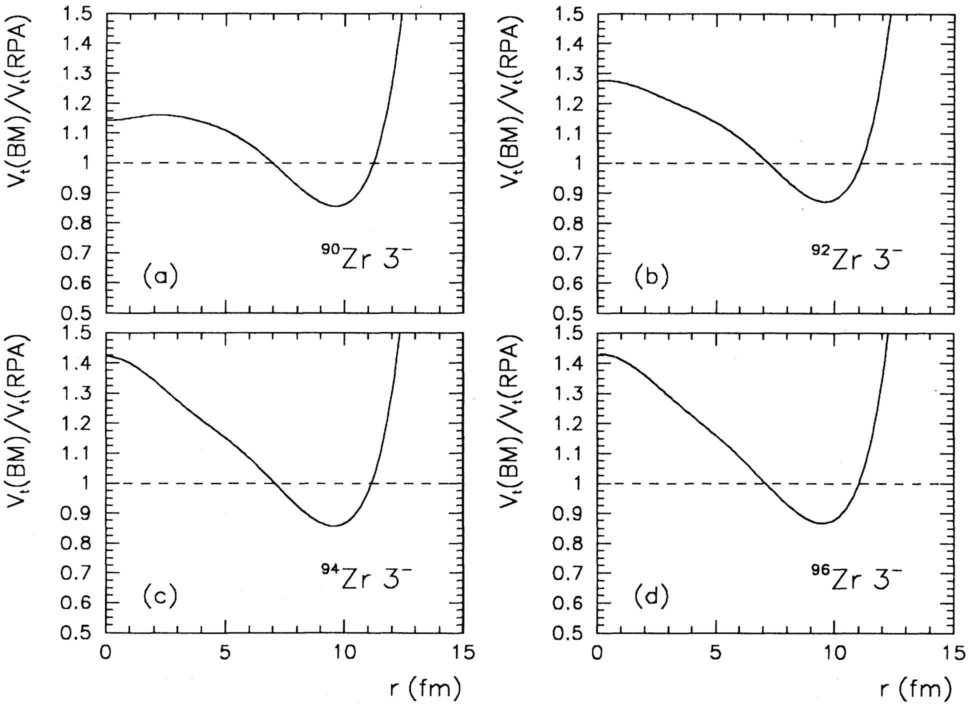

FIG. 13. Ratio of the real part of the BM to RPA transition potentials for exciting the 3_1^- states of ^{90,92,94,96}Zr. Note that the BM transition potential is smaller than the RPA transition potential for 7 fm$\lesssim r \lesssim$ 11 fm, the dominant region where the scattering interaction takes place.

DOMP calculations. The best values of δ_2^N and $B(E2)\uparrow$ are listed in Table VII.

The cross sections for exciting the 3_1^- states mainly determine δ_3^N and are very weakly dependent upon the $B(E3)\uparrow$. We used a procedure similar to the DOMP analysis of the 3_1^- states to deduce the values of δ_3^N and to determine the upper and lower limits of $B(E3)\uparrow$. In Fig. 15, calculations of the cross sections using our deduced δ_3^N and the $B(E3)\uparrow$ values adopted in [6] are compared to the data. Also shown for the 3_1^- state of ^{96}Zr are calculations with $B(E3)\uparrow= 0.120$ (solid curve) and $0.180e^2b^3$ (dashed curve) in order to demonstrate the sensitivity of the cross sections to the $B(E3)\uparrow$ values. The 3_1^- calculations also exhibit phase shifts relative to the data similar to those observed in the DOMP calculations.

c. Investigation of phase shifts. Several calculations were performed in an attempt to understand the phase shifts with respect to the data. In a study of the data of Rychel *et al.* [1], Satchler found that there was about

TABLE VII. Summary of DOMP and BM folding results. For the 3_1^- states, we give the range of $B(E3)\uparrow$ supported by the data (see text).

	DOMP			BM folding			
Isotope	$B(El)\uparrow$ (e^2b^l)	δ_l^N (fm)	M_n/M_p	$B(El)\uparrow$ (e^2b^l)	δ_l^N (fm)	M_n/M_p	N/Z
2_1^+ states							
^{90}Zr	0.063±0.005	0.400±0.020	0.84±0.12	0.063±0.005	0.440±0.022	1.04±0.13	1.25
^{92}Zr	0.075±0.010	0.673±0.034	1.93±0.24	0.080±0.010	0.758±0.038	2.22±0.26	1.30
^{94}Zr	0.058±0.010	0.632±0.032	2.21±0.32	0.060±0.010	0.671±0.034	2.39±0.33	1.35
^{96}Zr	0.025±0.005	0.589±0.030	3.70±0.53	0.022±0.005	0.621±0.031	4.34±0.67	1.40
3_1^- states							
^{90}Zr	0.051−0.091	0.750±0.038	0.75±0.09[a]	0.051−0.091	0.947±0.047	1.31±0.11[a]	1.25
^{92}Zr	0.047−0.087	0.831±0.042	1.07±0.10[a]	0.047−0.087	1.024±0.051	1.68±0.13[a]	1.30
^{94}Zr	0.067−0.107	0.932±0.047	1.11±0.11[a]	0.067−0.107	1.124±0.056	1.68±0.13[a]	1.35
^{96}Zr	0.080−0.160	1.111±0.056	1.22±0.11[a,b]	0.060−0.180	1.330±0.067	1.82±0.12[a,c]	1.40

[a] M_n/M_p calculated assuming the $B(E3)\uparrow$ given in the third column of Table VI, adopted from [5,6]. These values do not include the uncertainties of the $B(E3)\uparrow$.

[b] Using $B(E3)\uparrow= 0.180 \pm 0.018e^2b^3$ gives $M_n/M_p = 0.81 \pm 0.13$.

[c] Using $B(E3)\uparrow= 0.180 \pm 0.018e^2b^3$ gives $M_n/M_p = 1.30 \pm 0.16$.

a 1° phase shift between calculations of inelastic cross sections for exciting the 2_1^+ states in ^{92,96}Zr using the DOMP and folding models [16]. The present calculations do not show such a shift, and, in fact, the two models give nearly identical cross sections.

Coupled channels calculations which included coupling to the 3_1^- and 2_2^+ states, as well as reorientation, can cause shifts of the order of 0.5°. However, it is not at all clear whether the magnitudes of the reorientation coupling parameters required to effect such a phase shift are realistic.

Another possible way to effect such a phase shift is to assume that the potential in the outgoing channel is different from that for the incoming channel. This would be justified if the density distributions of the excited states were different from those of the ground states. To investigate this possibility, we assumed that the density distributions of the excited states were similar to those of the ground state but with different diffusenesses. (We could have obtained the same result by adjusting the radius instead.) The diffuseness parameter was adjusted until the folded potential for the outgoing channel caused the desired shift between the calculated and measured cross sections. The transition density was again taken to be of the BM form and the transition potential recalculated assuming the diffuseness for the transition density to be the average of the diffusenesses of the ground and excited states.

Fits to the inelastic data using this procedure are shown in Figs. 16 and 17 for the 2_1^+ and 3_1^- states, respectively. The δ_l^N and $B(El)\uparrow$ values are essentially the same as those listed in Table VII which were obtained from the fits to the data using BM transition densities. The changes in the diffusenesses that are required to account for the observed phase shifts are listed in Table VIII. The changes in diffuseness vary from -10% for the

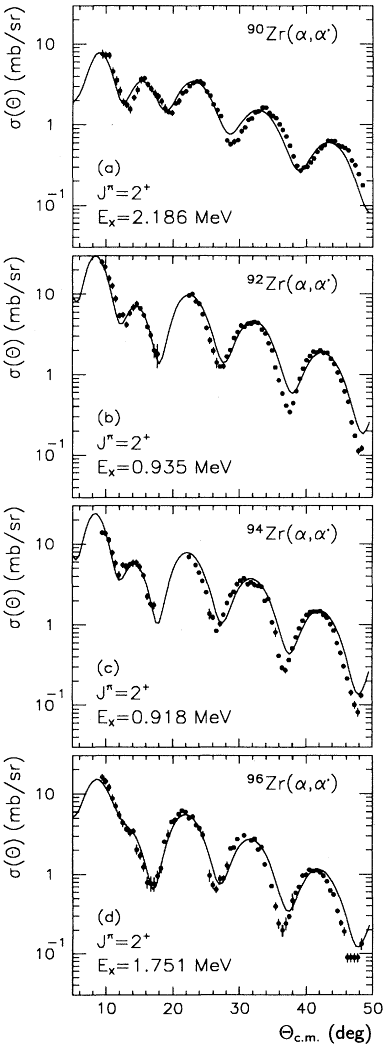

FIG. 14. Results of fits to data using folding model calculations with the BM transition densities for the 2_1^+ states of ^{90,92,94,96}Zr. The extracted values for $B(E2)\uparrow$, δ_2^N and M_n/M_p are shown in Table VII.

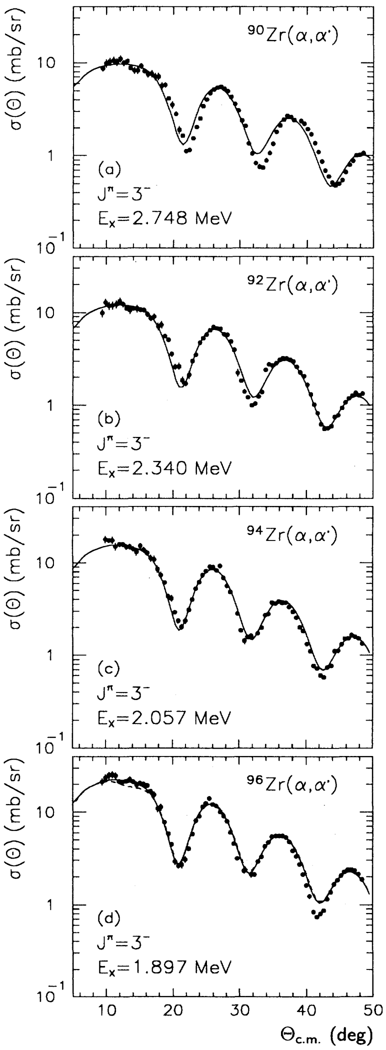

FIG. 15. Results of fits to data using folding model calculations with the BM transition densities for the 3_1^- states of ^{90,92,94,96}Zr. The extracted values for $B(E3)\uparrow$, δ_3^N, and M_n/M_p are shown in Table VII. For ^{96}Zr, the solid curve was calculated using $B(E3)\uparrow= 0.120e^2b^3$, while the dashed curve was calculated using $B(E3)\uparrow= 0.180e^2b^3$.

TABLE VIII. Diffuseness parameters of the BM ground state and excited state density distributions required to reproduce the phase of the cross sections at large angles. The radii of the distributions are given in Table IV, while the strengths of the effective alpha-nucleon interaction are given in Table V. The diffuseness of the transition density was taken as the average of the diffuseness parameters of the ground and excited state density distributions.

	Ground state		Excited state	
Isotope	a (fm)	RMS radius (fm)	a (fm)	RMS radius (fm)
2_1^+ states				
^{90}Zr	0.519	4.258	0.460	4.163
^{92}Zr	0.529	4.302	0.590	4.410
^{94}Zr	0.539	4.340	0.620	4.487
^{96}Zr	0.549	4.385	0.650	4.571
3_1^- states				
^{90}Zr	0.519	4.258	0.410	4.090
^{92}Zr	0.529	4.302	0.529	4.302
^{94}Zr	0.539	4.340	0.560	4.376
^{96}Zr	0.549	4.385	0.580	4.439

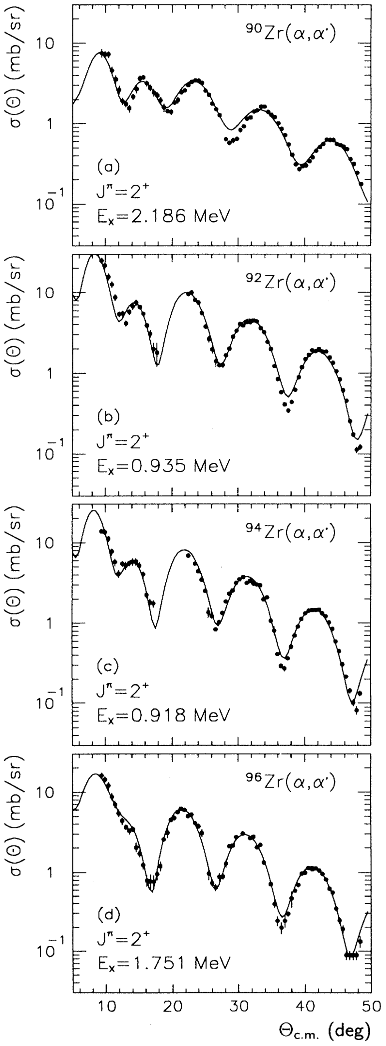

FIG. 16. Results of fits to data using folding model calculations with the BM transition densities for the 2_1^+ states of ^{90,92,94,96}Zr. The diffuseness parameter of the inelastic channel was varied in order to match the phase of the data at large angles. These diffuseness parameters are shown in Table VIII.

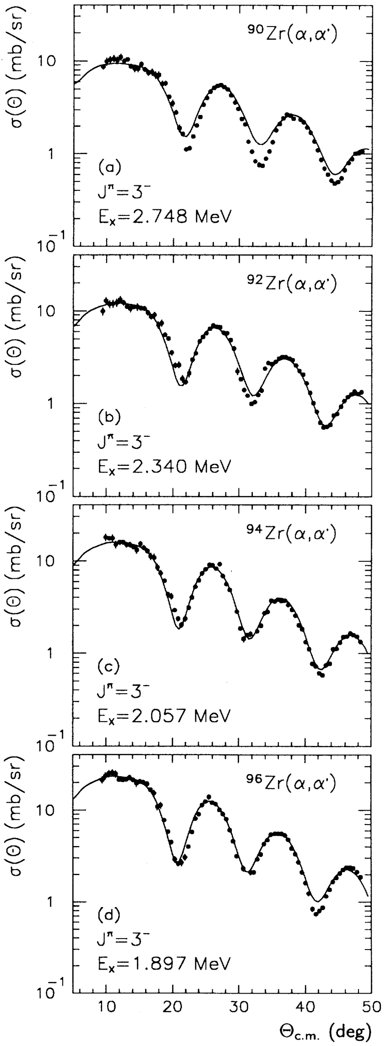

FIG. 17. Results of fits to data using folding model calculations with the BM transition densities for the 3_1^- states of ^{90,92,94,96}Zr. The diffuseness parameter of the inelastic channel was varied in order to match the phase of the data at large angles. The diffuseness parameters are shown in Table VIII.

2_1^+ state of ^{90}Zr to +18% for the 2_1^+ state in ^{96}Zr. These would translate into changes of the mean square radius of about 2–4 %, which is probably somewhat unphysical. Except for the 3_1^- state in ^{90}Zr, a smaller change in diffuseness is required for the 3_1^- states than is required for the 2_1^+ states in order to match the data.

IV. DISCUSSION AND CONCLUSIONS

By using Eqs. (6)–(9), the ratio of M_n/M_p can be calculated from the deduced quantities δ_l^N and δ_l^p as

$$M_n/M_p = \frac{A\delta_l^N}{Z\delta_l^p} - 1 \ . \tag{16}$$

For the zirconium isotopes, where $A/Z \approx 2.3$, it is clear from Eq. (16) that the uncertainties in the determination of M_n/M_p are approximately twice those of the δ_l. As can be seen in Table III, the agreement between the DOMP analyses of the data of Rychel *et al.* [1] and the present data is quite good; the mean values of the δ_l^N (except for the 2_1^+ state of ^{90}Zr) differ by 10%, which is about the uncertainty in the measured cross sections. Our δ_l^N for the 2_1^+ states (except for ^{90}Zr) are about 20% larger than those deduced from the ^{6}Li scattering [6], and about 10% larger for the 3_1^- states. Part of the disparity in the values of δ_l^N for the 2_1^+ states could be due to the differences in the $B(E2)\uparrow$ values between the alpha-particle and ^{6}Li data. Our $B(E2)\uparrow$ values deduced for ^{90,92}Zr (given in Table VII) are in excellent agreement with the corresponding values adopted from Coulomb excitation measurements [14], and for the 2_1^+ state in ^{94}Zr we obtain $B(E2)\uparrow = 0.058 \pm 0.010 e^2b^2$ in good agreement with a value $0.060 \pm 0.004 e^2b^2$ obtained from a recent lifetime measurement [13].

We believe that a more meaningful comparison is that between the DOMP and folding model analysis as shown in Table VII. Here it is found that the δ_l^N from the folding analyses are about 5–10 % larger than those from the DOMP analyses for the 2_1^+ states and about 20% larger for the 3_1^- states. This is about what would be expected from the nonequivalency between the DOMP and folding models for a BM-type transition density [3].

In Table VII we compare the M_n/M_p ratios obtained from the two types of analyses. Since the $B(El)\uparrow$ values are about the same for both methods, the relative M_n/M_p ratios differ by about 2.3 times the relative δ_l^N ratios. The two methods give comparable M_n/M_p for the 2_1^+ states which (except for ^{90}Zr) are about 50% or more larger than those reported in the ^{6}Li work. Furthermore, the M_n/M_p for the 2_1^+ states of ^{92,94,96}Zr are considerably larger than those for a "pure" isoscalar transition, i.e., N/Z. The larger values of δ_l^N deduced in this work are mainly responsible for the larger M_n/M_p ratios determined here. In the case of ^{96}Zr, the much smaller value of $B(E2)\uparrow$ causes an additional discrepancy between the M_n/M_p ratios. The large $M_n/M_p = 4.34 \pm 0.67$ for ^{96}Zr and the low $B(E2)\uparrow = 0.022 \pm 0.005 e^2b^2$ suggest that this 2_1^+ state is predominantly a neutron excitation. This is rather surprising and is contrary to the nuclear structure calculations of which we are aware. If true, it would suggest some strong interaction between the closed $d_{5/2}$ subshell neutrons and the valence protons. On the other hand, these results might simply be indicative that the 2_1^+ excitation in ^{96}Zr does not have a collective-type transition density, in which case utilization of either the DOMP or our folding model would be incorrect. Information pertaining to the form factor for this state could be attained by either inelastic electron scattering or intermediate energy proton scattering.

The folding model $M_n/M_p = 1.31 \pm 0.11$ for the 3_1^- state in ^{90}Zr already suggests that the transition is nearly isoscalar, contrary to the smaller $M_n/M_p = 0.75 \pm 0.09$ value deduced from the DOMP analysis. The trend of M_n/M_p for the 3_1^- states is similar to that predicted by the RPA calculation [6], except the folding model values indicate that the transitions have $M_n/M_p \approx N/Z$. Use of the recently measured value $B(E3)\uparrow = 0.180 \pm 0.018 e^2b^3$ [15] for the 3_1^- state of ^{96}Zr would give $M_n/M_p = 1.30 \pm 0.16$, which is in excellent agreement with a folding model using a BM-type transition density with the ^{6}Li data [15]. Since there is some uncertainty as to the values of $B(El)\uparrow$ for the other isotopes, one should not put too much weight upon their M_n/M_p values reported here.

In conclusion, we have measured elastic and inelastic cross sections for scattering of 35.4 MeV alpha particles by ^{90,92,94,96}Zr. The data were analyzed using both microscopic and macroscopic means. In the macroscopic analysis, the elastic scattering cross sections were fit using an optical potential of the Woods-Saxon form; the inelastic cross sections were analyzed using the deformed generalization of the optical potential (DOMP). In the microscopic analysis an effective alpha-nucleon interaction having a Gaussian shape was used. The strengths of the interaction were found by fitting the elastic data; the interaction was then folded with transition densities in order to predict the inelastic cross sections. Transition densities from RPA calculations as well as a Bohr-Mottelson form for the transition density were used. Our DOMP analyses give δ_l^N and $B(El)\uparrow$ values in good agreement with an earlier alpha-scattering study [1]. The δ_l^N also agree well with those deduced from ^{6}Li scattering [6]. Comparison of the δ_l^N deduced from DOMP fits versus folding model fits to the present data clearly show the inconsistency [3] between the two methods. The sensitivity of the deduced δ_l^N with respect to assumed transition densities has been demonstrated, as has the need for independent precision measurements of $B(El)\uparrow$. The rather large values of M_n/M_p and the implied strong isovector-isoscalar mixing deduced for transitions to the 2_1^+ states of ^{92,94,96}Zr certainly raise questions about the validity of using BM collective-type transition densities, as well as currently available nuclear structure calculations. The phase shifts between the oscillations in the experimental and calculated inelastic angular distributions also require further investigation.

ACKNOWLEDGMENTS

We would like to thank Dr. P. Parker and Dr. K. Hahn for their assistance during the early stages of this research. This research was sponsored by the U.S. Department of Energy under Contract No. DE-AC05-84OR21400 with Martin Marietta Energy Systems, Inc., and Grant No. DE-FG02-91ER-40609 at Yale University.

[1] D. Rychel, R. Gyufko, B. van Krüchten, M. Lahanas, P. Singh, and C. A. Wiedner, Z. Phys. A **326**, 455 (1987).

[2] G. J. Wagner, D. Grabmayr, and H. R. Schmidt, Phys. Lett. **113B**, 447 (1982).

[3] J. R. Beene, D. J. Horen, and G. R. Satchler, Phys. Rev. C **48**, 3128 (1993); D. J. Horen, J. R. Beene, and G. R. Satchler, Phys. Lett. B **316**, 463 (1993).

[4] Y. Wang and J. Rapaport, Nucl. Phys. **A517**, 301 (1990); Z. Phys. A **331**, 305 (1988).

[5] D. J. Horen, R. L. Auble, J. Gomez del Campo, R. L. Varner, J. R. Beene, G. R. Satchler, B. Lund, V. R. Brown, P. L. Anthony, and V. A. Madsen, Phys. Lett. B **296**, 18 (1992).

[6] D. J. Horen, R. L. Auble, J. Gomez del Campo, G. R. Satchler, R. L. Varner, J. R. Beene, B. Lund, V. R. Brown, P. L. Anthony, and V. A. Madsen, Phys. Rev. C **47**, 629 (1993).

[7] G. R. Satchler, *Direct Nuclear Reactions* (Oxford University Press, New York, 1983).

[8] A. Bohr and B. R. Mottelson, *Nuclear Structure* (Benjamin, New York, 1975), Vol. 2.

[9] B. Lund, Ph.D. thesis, Yale University (1995).

[10] V. R. Brown, J. A. Carr, V. A. Madsen, and F. Petrovich, Phys. Rev. C **37**, 1537 (1988).

[11] M. H. Macfarlane and S. C. Pieper, Argonne National Laboratory Report No. ANL-76-11, 1978 (unpublished); M. Rhoades-Brown, M. H. Macfarlane, and S. C. Pieper, Phys. Rev. C **21**, 2417 (1980); **21**, 2436 (1980).

[12] G. R. Satchler, Nucl. Phys. **A472**, 215 (1987).

[13] D. J. Horen, R. L. Auble, C. Y. Wu, D. Cline, M. Devlin, R. Ibbotson, and M. W. Simon, Phys. Rev. C **48**, 433 (1993).

[14] S. Raman C. H. Malarkey, W. T. Milner, C. W. Nestor, and P. Stelson, At. Data Nucl. Data Tables **36**, 1 (1987).

[15] D. J. Horen, R. L. Auble, G. R. Satchler, J. R. Beene, I. Y. Lee, C. Y. Wu, D. Cline, M. Devlin, R. Ibbotson, and M. W. Simon, Phys. Rev. C **48**, R2131 (1993).

[16] G. R. Satchler, Nucl. Phys. **A491**, 413 (1989).

[17] R. H. Spear, At. Data Nucl. Data Tables **42**, 55 (1989).